# Microstructure evolution in zirconium carbide thin films at different substrate temperatures

A. Heidarnia , Hamid Ghomi

**Abstract**

Zirconium carbide (ZrC) is promising candidate materials in advanced nuclear reactors as fuel cladding and plasma facing materials. It can employ to increase ductility and fracture toughness of tungsten as prominent candidate of plasma facing materials in ITER and DEMO future fusion reactors. In this study, ZrC thin films were deposited through DC magnetron sputtering at different substrate temperatures. Argon and acetylene are respectively employed as the sputtering gas and reaction gas to produce ZrC from a Zr target. The phase and structure, crystallite size, displacement density, microstrain, and lattice's constant of the produced thin films were determined using X-ray diffraction (XRD) analysis. Raman spectroscopy was also used to identify various structures and chemical bonds. Furthermore, the analysis of Raman peaks associated with amorphous carbon bonds revealed that the ratio of sp3/sp2 carbon bonds increases by increasing temperature from 100 °C to 180 °C, which substantially affects the hardness of the thin films. Field Emission Scanning electron microscopy (FESEM) was used to measure the cross-sectional area and thickness of the thin films, and it was discovered that increasing temperature enhances the thickness of the thin films. The elemental analysis of ZrC thin films that was performed using X-ray energy dispersive spectroscopy (EDS) demonstrated the atoms that constitute the thin film, and their changes with temperature variations.

**Keywords**

Microstructure, Zirconium carbide, Thin film deposition, Substrate temperature, Plasma facing materials.

*Laser and Plasma Research Institute, Shahid Beheshti University, Evin 1983963113, Tehran, Iran*
***Corresponding author**: h-gmdashty@sbu.ac.ir

## 1. Introduction

ZrC is a member of the high-temperature ceramic family. This ceramic is used in a wide range of industries, including cutting tools, hypersonic vehicles, high-temperature nuclear reactors, electronics, and other applications, due to its important and prominent properties, such as high melting point (approximately 3500°C), low cross-sectional absorption of thermal neutrons, high hardness, low working function of electron emission, metal behavior in electrical and optical properties, and so on. [1–4].

Various techniques have been used to produce ZrC thin films, e.g., electron beam evaporation, chemical vapor deposition (CVD) [5,6], pulsed laser ablation [7], and magnetron sputtering [8]. Numerous investigations have also been carried out on the different potentials and properties of ZrC thin films, and a number of parameters affecting the development of the films. R. Liu et al. [9] reviewed the development of the W-ZrC alloy for plasma facing materials for fusion devices. They perceived that ZrC operating as Oxygen getter at grain boundaries of tungsten and improved the strength, ductility, high temperature stability and resistance to neutron and ions irradiation. Also, the grain boundaries strengthening of tungsten reviewed by X. Wu et al. [10] and they realized by adding second phase ameliorated performance of tungsten. S. Biira et

al. [11] studied the effect of thermal behavior of ZrC thin films produced by chemical vapor deposition at various annealing temperatures on their performance. After annealing, they discovered that the lattice's constant and crystallite size increase. Furthermore, depending on the crystalline preference, the surface morphology and hardness of the produced thin film vary depending on the annealing temperature. J. Xu et al. [12] used a twin cathode glow discharge to create a ZrC nanocrystalline film on a titanium-aluminum-vanadium (Ti-6Al-4V) alloy in order to improve its corrosion resistance. They revealed that the corrosion resistance of the coating decrease by increasing temperature. According to Meng et al. [13], who investigated a coating of ZrC by magnetron sputtering at different methane to argon ratios, the transition from the crystalline to the amorphous phase occurs when the carbon concentration exceeds 86%. Additionally, a high proportion of carbon reduces hardness, and improves the friction coefficient and corrosion resistance of the coating.

In the current research for further investigate the ZrC thin film properties, focused on the structure, amorphous carbon bonds, and element composition evolution of ZrC thin films produced by DC magnetron sputtering at the substrate temperatures of 100°C, 150°C, and 180°C. XRD analysis and the Scherer method were used to investigate the crystallite size, microstrain, displacement density, and lattice's constant
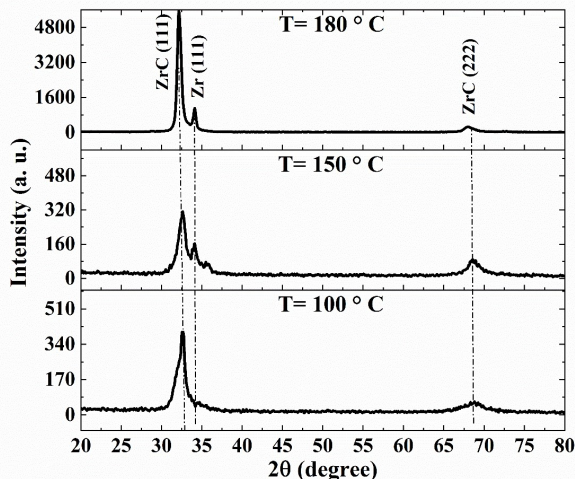
**Figure 1.** The XRD pattern of ZrC thin films at three different substrate temperatures.



**Figure 2.** Crystallite size and FWHM changes along (111) ZrC crystal plane.

at the aforementioned temperatures. Besides, the chemical bonds in ZrC coatings, as well as the evolution of amorphous carbon bonds, were examined using Raman analysis. And the evolution of elemental composition at different temperatures was detected using EDS analysis.

## 2. Experimental method

DC magnetron sputtering was used to deposit ZrC coatings on Si substrates at the temperatures of 100°C, 150°C, and 180°C. This method utilized a Zr target with a diameter of 5 cm, a thickness of 3 mm, and a purity of 99.95%, argon as the sputtering gas (Ar, 5N), and acetylene as the reactive gas ($C_2H_2$, 5N) in the process. The substrates were first cleaned through washing by soap and water, followed by ultrasonic washing in acetone and ethanol solutions for 20 minutes in each solution. After the substrates were dried in dry air, they were placed inside the vacuum chamber. Rotary and turbo-molecular vacuum pumps evacuated the chamber to a pressure of $10^{-4}$ mbar. Pre-sputtering operations were carried out for 15 minutes to eliminate the possibility of contamination of the target surface by introducing Ar to the chamber and regulating the pressure in the range of $10^{-1}$ mbar. The system was then drained, and the argon-acetylene gas mixture was introduced into the chamber in a proportion equal to $C_2H_2/ C_2H_2+Ar=15$, after which the chamber pressure was adjusted to a value of $4 \times 10^{-2}$ mbar. By applying a voltage to the electrodes of the sputtering device, the gas inside the chamber was ionized and argon ions were generated and accelerated to the Zr target by an electric field between the electrodes and sputter zirconium atoms. These atoms were scattered in all directions and reacted with carbon atoms due to the decomposition of acetylene gas. Finally, the ZrC coating was formed on silicon substrates. The experimental conditions are shown in Table 1. To study the microstructure of ZrC thin films, an XRD de-
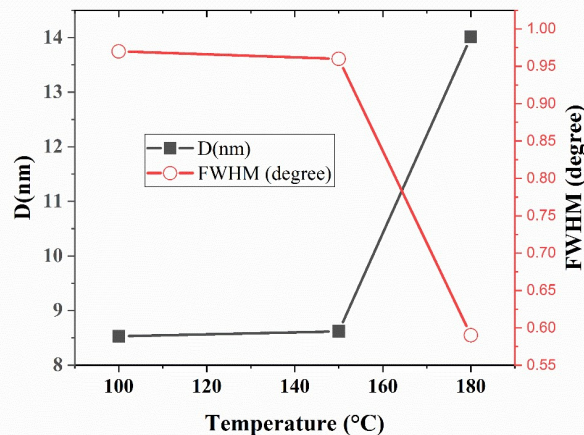
vice manufactured by STOE with a Cu k$\alpha$ X-ray generator having a wavelength of 1.54060 A°, a voltage of 40 kV and a current of 40 mA in the range of 20-80 ° was employed. A Takram P50C0R10 Raman spectrometer manufactured by Teksan with a laser having a wavelength of 532 nm and a power of 0.5-70 mW was utilized to study the structure and chemical bonds between carbon-zirconium and carbon-carbon. Additionally, a field emission scanning electron microscope (FESEM) equipped with X-ray energy dispersive spectroscopy (EDS) was used to evaluate the cross section and thickness of the thin films produced, as well as to analyze their elemental composition.

## 3. Results and discussion

### 3.1 X-ray diffraction

As illustrated in Fig. 1, the X-ray diffraction pattern of ZrC thin films generated at various substrate temperatures was investigated. It shows that the produced thin films are composed of two different phases of metal and ceramic. In ZrC, the ceramic phase can be detected at the diffraction angles of approximately ($2\theta$) 32.52 and 68.7, which correspond to two crystal planes of (111) and (222). Based on the International Commission on Crystallographic Data (ICCD), this pattern is in accordance with the standard X-ray diffraction pattern of the zirconium carbide card with the reference code of 01-074-1221, indicating that ZrC thin films have an FCC structure. Another finding is that, the peak of the diffraction pattern found at an angle of approximately ($2\theta$) 34.09 is associated with the metal zirconium phase, which corresponds to the crystal plane (111) and has an FCC lattice structure (ICCD standard zirconium X-ray diffraction card with the reference code of 01- 088-2329). As shown in Fig. 1, the peak intensity of (111) crystal plane of zirconium carbide grows as temperature increases, indicating that the crystallization of thin films is rising in this direction as temperature increases.
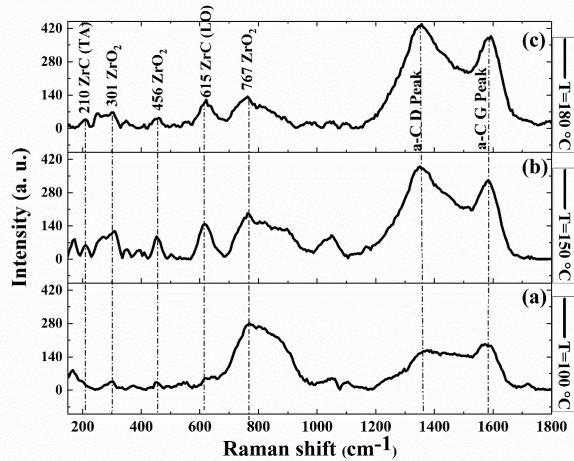
**Figure 3.** The Raman spectrum of ZrC thin films at the substrate temperatures of a)100°C, b) 150°C, and c) 180°C.



**Figure 5.** The variations of position and FWHM of G-peak at different substrate temperatures.

In this experiment, the crystal size ($D$) of ZrC in the direction of (111) crystal plane was estimated at three different temperatures using Scherer equation [14]. Scherer relationship is given in Eq. (1).

$$D = \frac{k\lambda}{\beta cos\theta} \quad (1)$$

Where $k$ denotes the crystal shape factor constant ($\sim$ 0.9), $\beta$ denotes the full width at half maximum (FWHM) in radians, $\theta$ denotes the Bragg's angle in degrees, and $\lambda$ denotes the wavelength of the X-ray source (1.5406 A$^o$). Figure 2 shows how the crystallite size of zirconium carbide thin films changes as the temperature of the substrate increases.

As the substrate temperature increases from 100°C to 180°C, FWHM decreases along (111) ZrC crystal plane, which increases the crystallite size (from 8.5 nm to 14 nm) (see Fig.
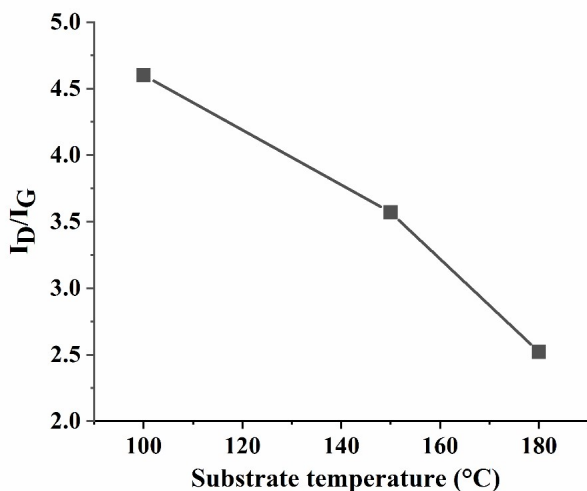
2). This is in agreement with [15]. As the substrate temperature increases from 100°C to 150°C, the crystallite size also slightly increases, i.e., from 8.5 nm to 8.6 nm. This range of temperatures sees the majority of the increase in energy spent on the addition of zirconium metal to zirconium carbide ceramic. At higher temperatures (up to 180°C), the phase structure is maintained at 150°C, and the additional heat generated causes crystallite growth from 8.6 to 14 nm to occur. Another parameter that depends on the crystallite size is the displacement density ($\delta$), which is defined as the length of dislocation lines per unit volume of the crystal and may be approximated using Eq. (2) [14, 16, 17].

$$\delta = \frac{1}{D^2} \quad (2)$$

Where $D$ is the crystallite size estimated using Eq. (1). Therefore, the lower the displacement density along the (111) crystal plane, the better the crystallization would be. Displacement densities along (111) ZrC crystal plane are given in Table 2 for three different temperatures. Similarly, the microstrain of ZrC thin films along (111) crystal plane is determined at different temperatures the basis of Eq. (3) [14]. The microstrain values calculated are shown in Table 2.

$$\varepsilon = \frac{\beta}{4\tan\theta} \quad (3)$$

Considering the X-ray diffraction patterns of ZrC discussed above, their crystal lattice is cubic. Therefore, Eq. (4) is used to determine the cubic lattice's constant along (111) ZrC crystal plane [18].

$$a_{cubic} = d_{hkl} \times \sqrt{h^2 + k^2 + l^2}, d_{hkl}(Bragg's law) = \frac{n\lambda}{2\sin\theta} \quad (4)$$

In Eq. (4), $a_{cubic}$ is the cubic lattice's constant in A°, $d_{hkl}$ is the distance between crystal planes, and $hkl$ is the miller



**Figure 4.** Changes of D to G peak Intensity at different substrate temperatures.
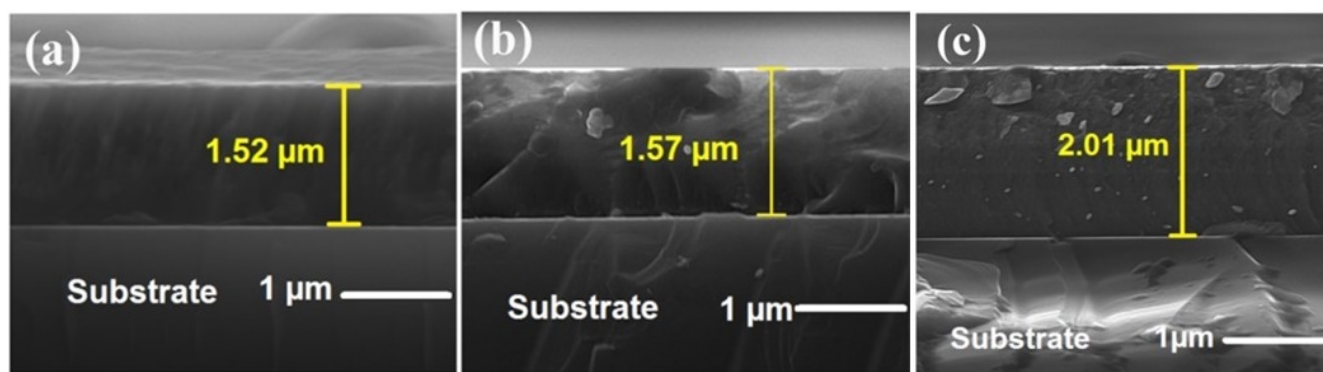
**Figure 6.** The cross-sectional FESEM images of ZrC thin films on Si substrate at a)100°C, b) 150°C, and c) 180°C.

index. The lattice's constant calculated along (111) ZrC (111) crystal plane at three different temperatures is given in Table 2.

Therefore, as temperature increases, the microstrain and displacement density decrease, but the lattice's constant increases. Consequently, minimum microstrain, minimum displacement density, and maximum crystallite size are obtained at 180°C, indicating the best mode of crystallization.

### 3.2 Raman spectroscopy

Figure 3 depicts the Raman spectrum of ZrC thin films that were grown on the substrates at the temperatures of 100°C, 150°C and 180°C. The Raman active peaks observed in ZrC are located in the frequency range of 190-620 cm$^{-1}$, and amorphous carbons (a-C) are responsible for the Raman active peaks observed in ZrC in the frequency range of 1300-1600 cm$^{-1}$ [19]. ZrC peaks are observed at 210 cm$^{-1}$ and 615 cm$^{-1}$, demonstrating that ZrC is polycrystalline and is assigned to TA (transverse acoustic) and LO (longitudinal acoustic) [19]. The Raman peaks observed at 301, 456, and 767 cm$^{-1}$ are assigned to ZrO$_2$ [20, 21]. The amorphous carbon (a-C) Raman peaks, which are known as D-peak (diamond or disorder peak) and G-peak (graphite peak), are located at 1300-1400 cm$^{-1}$ and 1550-1600 cm$^{-1}$.

In the thin films containing carbon atoms, the position and FWHM of G-peak, and ID/IG (the ratio of D-peak to G-peak Intensity) are important parameters providing information about the structure and type of their chemical bond and the sp$^2$/sp$^3$ hybridization ratio. The value of ID/IG, which is proportional to the ratio of sp$^2$/sp$^3$ carbon bonds, is obtained using the area under the D-peak to G-peak fitting curve [22], and its value is equal to 4.6 at the substrate temperature of 100°C and decreases as temperature increases in such a way that it reaches 2.52 at 180°C (see Fig. 4). Hence, as temperature increase, the ratio of sp$^2$/sp$^3$ decreases (the ratio of sp$^3$/sp$^2$ increases). This is in agreement with the research conducted by X. Zhao et al. [23], indicating that an increase in the substrate temperature plays a pivotal role in producing hard carbon coatings (having more sp$^3$ carbon bonds). It should be mentioned that the G-peak position depends on the amount of sp$^2$ carbon and its FWHM depends on the amount of sp$^3$ carbon [24]. The position and FWHM changes of G-peak are shown in Fig. 5, signifying the increase in disorder by increasing temperature. These changes in the range of 100-180°C are in agreement with the research of Mingming Li et al. [24] conducted in the range of 100-200°C.//
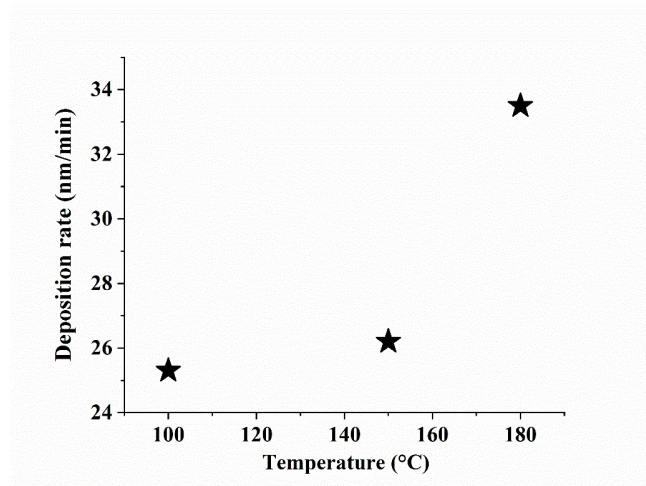
### 3.3 Field-Emission scanning electron microscopy (FESEM)

Figure 6 shows cross-sectional images of ZrC thin films at three distinct substrate temperatures of 100°C, 150°C, and 180°C. It is shown that the thickness of ZrC thin films increases from 1.52 µm to 2.01 µm as temperature increases. This is in agreement with the XRD results (see Fig. 2), which



**Figure 7.** ZrC deposition rate at different temperatures.

**Table 1.** Zirconium carbide coating conditions on silicon substrates.

| Sample code | Substrate temperature (°C) | Power (W) | Working pressure (mbar) | Deposition time (h) | Substrate-target distance (cm) | Gas ratio C$_2$H$_2$ / C$_2$H$_2$+ Ar |
|---|---|---|---|---|---|---|
| ZrC1 | 100 | 150 | 4×10$^{-2}$ | 1 | 8 | 15 |
| ZrC2 | 150 | 150 | 4×10$^{-2}$ | 1 | 8 | 15 |
| ZrC3 | 180 | 150 | 4×10$^{-2}$ | 1 | 8 | 15 |

**Table 2.** The estimated Parameters resulting from the analysis of ZrC thin film structures along (111) crystal plane using Scherer method.

| Sample code | Substrate temperature (⁰C) | Crystallite size (nm) | Lattice's constant (A°) | Dislocation density δ(×10$^{12}$ cm$^{-2}$) | Microstrain ε(×10$^{-5}$) |
|---|---|---|---|---|---|
| ZrC1 | 100 | 8.5 | 4.77 | 1.37 | 1.45 |
| ZrC2 | 150 | 8.6 | 4.77 | 1.34 | 1.43 |
| ZrC3 | 180 | 14 | 4.81 | 0.5 | 0.89 |

**Table 3.** EDS analysis of ZrC thin films at the different temperatures.

| Sample code | Substrate temperature (⁰C) | Elemental composition (in weight%) | | Elemental composition (in atomic%) | |
|---|---|---|---|---|---|
| | | C | Zr | C | Zr |
| ZrC1 | 100 | 15.13 | 80.23 | 54.66 | 38.16 |
| ZrC2 | 150 | 9.79 | 85.32 | 42.35 | 48.61 |
| ZrC3 | 180 | 3.34 | 91.22 | 18.92 | 67.94 |

revealed that the crystallite size grows by increasing temperature.

The changes of the thin film thickness in the range of 100-150°C are lower than in the range of 150- 180°C. The reason can be found in the XRD pattern of thin films at three differ-

ent temperatures. As shown in Fig. 1, the diffraction pattern at 100°C includes only the ceramic phase, but at 150°C and 180°C, it includes both ceramic and metal phases. For that reason, in the first temperature range, a major part of the energy resulting from the increase in temperature is used to change the phase structure of the thin film, but in the second temperature range, the whole energy resulting from the increase in temperature is used to grow the crystallite and increase the film thickness.

According to the thickness of the ZrC thin films measured by FESEM, and the deposition duration (1 hour), the deposition rate is obtained at three different temperatures as shown in Fig. 7.

### 3.4 X-ray energy dispersive spectroscopy (EDS)

To evaluate the elements comprising the thin film, X-ray EDS was used. The EDS spectrum of ZrC thin films at three different temperatures of 100°C, 150°C, and 180°C are shown in Fig. 8.

The results of EDS (see Table 3) verify the presence of Zr, C, and Si elements, where Zr and C constitute the thin films, and Si constitutes the substrate. All the same, the gas ratio used in the ZrC deposition is the same at three different temperatures, but the concentration and atomic percentage of the elements are different. The concentration of carbon reduces as the temperature rises from 100°C to 180°C, while the concentration of zirconium increase Temperature variations from 100°C to 200°C in Mingming Li et al. [24] show that silicon and carbon components in the silicon carbide coating vary.



**Figure 8.** The EDS spectrum of ZrC thin films at three different temperatures of a)100°C, b) 150°C, and c) 180°C.

## 4. Conclusion

ZrC thin films were deposited on Silicon substrate at three different temperatures of 100°C, 150°C, and 180°C at the gas ratio of $C_2H_2/Ar+C_2H_2$=15. With the help of XRD patterns and using Scherer method, it was identified that the produced thin films have a cubic lattice, and as temperature increased from 100°C to 180°C, both the lattice's constant and the crystallite size increased from 4.7708 A° to 4.8140 A°, and from 8.6nm to 14nm, respectively. Moreover, as temperature increased, the displacement density and microstrain of the thin films decreased, so minimum displacement density ($0.5×10^{12}$ cm$^{-2}$) and minimum microstrain ($0.89×10^{-5}$) were obtained at 180°C. Raman spectroscopy verified the presence of TA and LO modes in ZrC at 210 cm$^{-1}$ and 615 cm$^{-1}$
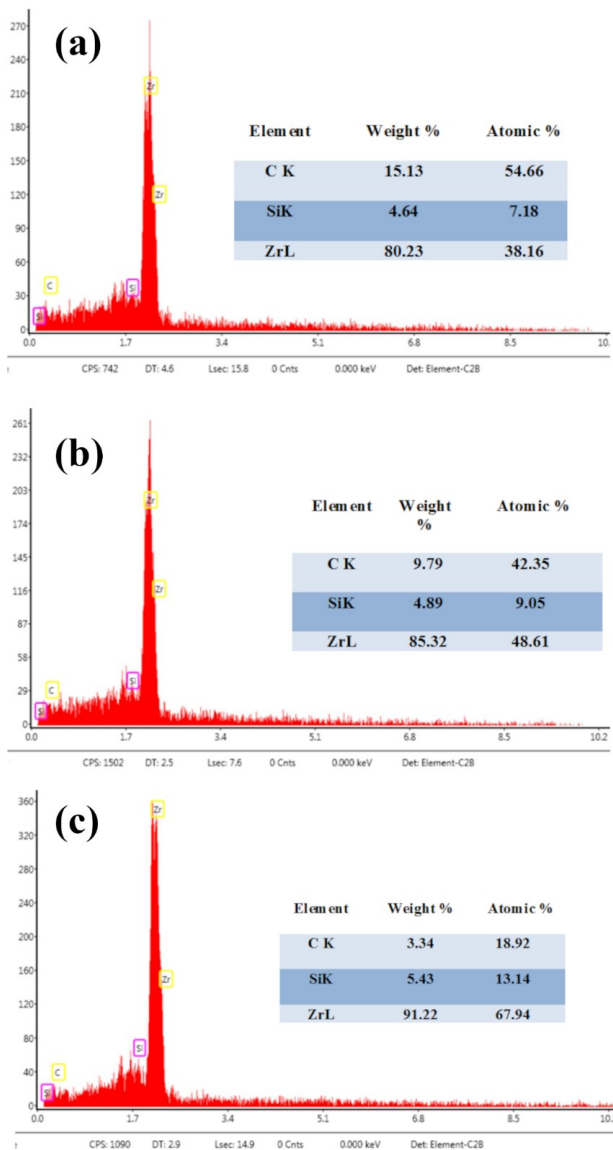
, respectively. Furthermore, the D-peak and G-peak analyses of carbon bonds showed that ID/IG decreases as temperature increases. The FESEM images also showed that the thickness of the thin films increases from 1.52μm to 2.01μm as temperature increases. The EDS results also showed that by increasing temperature, the density of carbon and Zr decreases and increases, respectively.

**Conflict of interest statement:**
The authors declare that they have no conflict of interest.

# References

[1] J. Aihara, S. Ueta, M. Honda, N. Mizuta, M. Goto, Y. Tachibana, and K. Okamoto. *Journal of Nuclear Materials*, **522**:32, 2019.

[2] V.V. Chayeuski, V.V. Zhylinski, P.V. Rudak, D.P. Rusalsky, N. Viˇsniakov, and O. ˇCernaˇšˇejus. *Applied Surface Science*, **446**:18, 2018.

[3] M. h. Ding, H.-S. Zhang, C. Zhang, and X. Jin. *Surface and Coatings Technology*, **224**:34, 2013.

[4] D.D. Kumar, G.S. Kaliaraja, A.M.K. Kirubaharan, K. Alagarsamy, V. Vishwakarma, and R. Baskaran. *Surface and Coatings Technology*, **374**:569, 2019.

[5] S.-L. Wang, K. z. Li, H.-J. Li, Y.-L. Zhang, and W.-Y. Zhang. *International Journal of Refractory Metals and Hard Materials*, **48**:108, 2015.

[6] Y. Zhu, L. Cheng, B. Ma, S. Gao, W. Fenga, Y. Liu, and L. Zhang. *Applied Surface Science*, **332**:591, 2015.

[7] D. Craciun, G. Socol, E. Lambers, E.J. McCumiskey, C.R. Taylor, C. Martin, N. Argibay, D.B. Tanner, and V. Craciun. *Applied Surface Science*, **352**:28, 2015.

[8] A. Gilewicz, K. Mydłowska, J. Ratajski, Ł. Szparaga, P. Bartosik, P. Kochmanski, and R. Jedrzejewski. *Vacuum*, **169**:108909, 2019.

[9] R. Liu, Z.M. Xie, J.F. Yang, T. Zhang, T. Hao, X.P. Wang, Q.F. Fang, and C.S. Liu. *Nuclear Materials and Energy*, **16**:191, 2018.

[10] X. Wu, X. Li, Y. Zhang, Y. Xu, W. Liu, Z. Xie, R. Liu, G.-N. Luo, X. Liu, and C.S. Liu. *Journal of Fusion Energy*, **39**:342, 2021.

[11] S. Biira, T.T. Thabethe, T.T. Hlatshwayo, H. Bissett, T. Ntsoane, and J.B. Malherbe. *Journal of Alloys and Compounds*, **834**:155003, 2020.

[12] J. Xu, Z. Li, S. Xu, P. Munroe, and Z.-H. Xie. *Journal of Power Sources*, **297**:359, 2015.

[13] Q.N. Meng, M. Wen, F. Mao, N. Nedfors, U. Jansson, and W.T. Zheng. *Surface and Coatings Technology*, **232**:876, 2013.

[14] R. Rai, T. Triloki, and B.K. Singh. *Applied Physics A*, **122**:938, 2016.

[15] L.C. Agudelo-Morimitsu, J. De La Roche, D. Escobar, R. Ospina, and E. Restrepo-Parra. *Ceramics International*, **39**:7355, 2013.

[16] A.R. Bushroa, R.G. Rahbari, H.H. Masjuki, and M.R. Muhamad. *Vacuum*, **86**:1107, 2012.

[17] S. Habashyani, A. Özmen, S. Aydogan, and M. Yilmaz. *Vacuum*, **157**:479, 2018.

[18] N.K. Das, J. Chakrabartty, S.F.U. Farhad, A.K. Sen Gupta, E.M.K. Ikball Ahamed, K.S. Rahman, A. Wafi, A.A. Alkahtani, M.A. Matin, and N. Amin. *Results in Physics*, **17**:103132, 2020.

[19] S. Pellegrino, P. Trocellier, L. Thomé, S. Miro, J.M. Costantini, and E. Jouanny. *Nuclear Instruments and Methods in Physics Research Section B: Beam Interactions with Materials and Atoms*, **454**:61, 2019.

[20] S.N. Basahel, T.T. Ali, M. Mokhtar, and K. Narasimharao. *Nanoscale Research Letters*, **10**:73, 2015.

[21] H. Zegtouf, N. Saoula, M. Azibi, L. Bait, N. Madaoui, M.R. Khelladi, and M. Kechouane. *Surface and Coatings Technology*, **393**:125821, 2020.

[22] Z. Li, H. Zhang, W. He, C. Ma, N. Xiangfan, G.a. Zhang, and Y. Li. *Ceramics International*, **47**:5730, 2021.

[23] X. Zhao, X. He, Y. Sun, J. Yi, and P. Xiao. *Acta Materialia*, **57**:893, 2009.

[24] M. Li, L. Jiang, Y. Sun, T. Xiao, P. Xiang, and X. Tan. *Journal of Non-Crystalline Solids*, **503-504**:252, 2019.